

Hydrocode modeling of oblique impacts: The fate of the projectile

E. PIERAZZO* AND H. J. MELOSH

Lunar and Planetary Laboratory, University of Arizona, Tucson, Arizona 85721, USA

*Correspondence author's e-mail address: betty@lpl.arizona.edu

(Received 1999 March 15; accepted in revised form 1999 September 20)

Abstract—All impacts are oblique to some degree. Only rarely do projectiles strike a planetary surface (near) vertically. The effects of an oblique impact event on the target are well known, producing craters that appear circular even for low impact angles ($>15^\circ$ with respect to the surface). However, we still have much to learn about the fate of the projectile, especially in oblique impact events. This work investigates the effect of angle of impact on the projectile.

Sandia National Laboratories' three-dimensional hydrocode CTH was used for a series of high-resolution simulations (50 cells per projectile radius) with varying angle of impact. Simulations were carried out for impacts at 90, 60, 45, 30, and 15° from the horizontal, while keeping projectile size (5 km in radius), type (dunite), and impact velocity (20 km/s) constant.

The three-dimensional hydrocode simulations presented here show that in oblique impacts the distribution of shock pressure inside the projectile (and in the target as well) is highly complex, possessing only bilateral symmetry, even for a spherical projectile. Available experimental data suggest that only the vertical component of the impact velocity plays a role in an impact. If this were correct, simple theoretical considerations indicate that shock pressure, temperature, and energy would depend on $\sin^2 \Theta$, where Θ is the angle of impact (measured from the horizontal). However, our numerical simulations show that the mean shock pressure in the projectile is better fit by a $\sin \Theta$ dependence, whereas shock temperature and energy depend on $\sin^{3/2} \Theta$. This demonstrates that in impact events the shock wave is the result of complex processes that cannot be described by simple empirical rules. The mass of shock melt or vapor in the projectile decreases drastically for low impact angles as a result of the weakening of the shock for decreasing impact angles. In particular, for asteroidal impacts the amount of projectile vaporized is always limited to a small fraction of the projectile mass. In cometary impacts, however, most of the projectile is vaporized even at low impact angles.

In the oblique impact simulations a large fraction of the projectile material retains a net downrange motion. In agreement with experimental work, the simulations show that for low impact angles (30 and 15°), a downrange focusing of projectile material occurs, and a significant amount of it travels at velocities larger than the escape velocity of Earth.

INTRODUCTION

Impacts have created enormous scars on the surfaces of nearly all solar system bodies. In past decades a large amount of work, both experimental and theoretical, has been devoted to understanding the details of the impact process. Scaling laws have been derived that describe impact crater size, shape, depth, ejecta, and melt deposits (e.g., Croft, 1985; Schmidt and Housen, 1987; Holsapple and Schmidt, 1987) as function of impactor size and type, velocity, and angle of impact. The fate of the impactor itself, however, has not received as much attention. During a high-speed impact, the impactor is completely destroyed. Parts are either melted or vaporized and often mixed with a much larger volume of target material. Consequently, it is very difficult to find parts of the projectile, or even its geochemical signature, on planetary surfaces after an impact. Laboratory experiments (Gault and Wedekind, 1978; Schultz and Gault, 1990a; Schultz and Sugita, 1996) showed a downrange focusing and acceleration of projectile (and target) material as the angle of impact decreases from the vertical. However, even in highly controlled laboratory experiments (e.g., Schultz and Gault, 1990a; Schultz and Sugita, 1996) it is difficult to follow the evolution of the projectile at hypervelocity speeds (i.e., >5 km/s, the typical speed of sound in the target).

The fate of the projectile in impact events is very important for our understanding of many aspects of impacts. A large projectile impacting a planetary surface can be a source for important

climatically active gases, like S, and H_2O (in the case of a cometary impact). This was dramatically demonstrated by the 1994 impact of comet Shoemaker–Levy 9 with Jupiter, when huge S-rich plumes (an estimated 10^{11} – 10^{14} g of S were released at the impact site of the G fragment alone; Noll *et al.*, 1995) were seen rising through Jupiter's atmosphere. Much of this S may have come from the comet fragment. Kring *et al.* (1996) estimate the amount of S that could be liberated from vaporized asteroids and comets that strike the Earth as a function of meteoritic composition and projectile diameter. They concluded that even relatively small asteroids, ~ 0.3 km in diameter, can inject the same amount of S into the stratosphere as the 1883 Krakatau eruption, with the potential for causing global climatic effects. According to Shoemaker (1983), such asteroids or comets impact the Earth at a rate of 1 per 10 000 years. Recently, the possibility of impact delivery of volatiles to planetary surfaces has received new confirmation with the discovery that even on the dry Moon there are deposits of water ice in permanently dark regions near the south pole (Nozette *et al.*, 1996; Feldman *et al.*, 1998).

The fate of the impactor in large impact events is also crucial for a better understanding of the origin and evolution of life in the solar system (e.g., Zahnle and Sleep, 1997). The possibility of transport and delivery of life or organic material among planetary objects of the solar system has received considerable attention in the past. However, a definitive answer as to how much organic material may

be delivered by impacts has not been reached yet, mainly because of the lack of accurate information on the pressures and temperatures in the projectile during impact events. A study of the thermodynamic history of the projectile can help us to understand if there is any possibility for survival of organic material at all (Chyba *et al.*, 1990; Thomas and Brookshaw, 1997; Pierazzo and Chyba, 1999). Furthermore, the possibility of the creation of "organic-rich ponds" (Clark, 1988) at an impact site depends on the organic material from the projectile being deposited within the crater. The "soft landing" hypothesis of Clark (1988) needs to be reinvestigated, recognizing that in oblique impacts the impactor has a substantial horizontal momentum even after it plunges into the surface.

Recent research on the K/T extinction has also focused attention on the projectile's fate. It was the realization that the Ir layer at the K/T boundary was indeed the signature of an extraterrestrial object (Alvarez *et al.*, 1980) that made it possible, for the first time, to connect a major terrestrial mass extinction to an impact event. Furthermore, the worldwide distribution of Ir from the projectile seemed to sustain the idea that most of the projectile vaporized in the impact. However, the suggestion that a piece of the K/T boundary impactor could have been found in sediments from the Pacific Ocean (Kyte, 1998) brings new questions on if and how any part of a projectile can survive an impact event and challenges the general belief that the impactor is completely melted or vaporized upon impacting a surface. It seems likely that the survival of projectile fragments depends on the fragment's original location within the projectile with respect to its flight path (*e.g.*, Schultz and Gault, 1990a). The fate of the Chicxulub impactor was the focus of work by Schultz and Sugita (1996), who carried out a series of laboratory experiments using the NASA Ames Vertical Gun Range. They found that in oblique impacts significant fractions of the impactor do not undergo vaporization or melting. Most of the impactor decouples from the later crater-forming process and retains a significant downrange momentum. They concluded that the vapor phase largely originates in the lower portion of the impactor during penetration, where it mixes with the target along the interface. The molten component of the projectile, on the other hand, follows a different trajectory from the vapor phase, ricocheting at low angles, and retaining a net downrange motion with velocities that exceed the initial impact velocity.

HYDROCODE MODELING

A series of high-resolution three-dimensional simulations were carried out, in collaboration with Dr. Crawford of the Sandia National Laboratories, using the three-dimensional hydrocode CTH (McGlaun *et al.*, 1990) coupled to the SESAME equation of state package (SESAME '83, 1983). The CTH code, developed at Sandia National Laboratories (Albuquerque, New Mexico), models multi-dimensional, multimaterial, large deformations, strong shock wave physics, and it can be used in one-, two-, and three-dimensions; the latter option, using bilateral symmetry, was used for the simulations presented here.

The simulations were constructed to model the Chicxulub impact event, in which a projectile ~5 km in radius strikes the target at an impact velocity of 20 km/s. Each run is characterized by a very high-resolution, 50 cells per projectile radius, corresponding to cells $100 \times 100 \times 100$ m in a cubic region, 16 km each side, centered on the impact point (only the $y > 0$ halfspace was defined in the simulations, because of the bilateral symmetry). A region of progressively lower resolution then follows, where the cell size is

increased by a factor of 1.05 from the previous cell. This results in a mesh of fifteen million cells, and the projectile alone, which is a spherical asteroid 10 km in diameter, is represented by over 260 000 cells (because only the $y > 0$ halfspace is modeled, only half of the projectile needs to be represented). Each simulation extends over 5 s, which is enough time for the shock wave to completely engulf the projectile and to be reflected back as a rarefaction wave, unloading the projectile from high pressure.

Available tabular (SESAME) equations of state were used for the simulations. We used dunite for the asteroid. Because these simulations model the Chicxulub impact event (*e.g.*, see Pierazzo and Melosh, 1999), the target composition reflects the stratigraphy of the Chicxulub impact site, in the Yucatán Peninsula, Mexico. Water is used to represent the shallow sea (100 m deep), calcite for the sedimentary layer (2.9 km deep), granite for the crust, and, finally, dunite is introduced to represent the mantle, below a depth of 33 km (*e.g.*, see Pierazzo *et al.*, 1998). Air was also inserted above the target to simulate the atmosphere.

Up to 1000 tracer particles were regularly distributed in both the target and the projectile. The tracers are massless particles that move through the mesh recording the thermodynamic history of given material points in time. Between 151 and 165 tracers are distributed inside the projectile in each simulation. Tracers were regularly distributed in rows originating at the projectile center and spaced by constant angular intervals of $\Delta\theta = 30^\circ$ and $\Delta\varphi = 30^\circ$ in the $y > 0$ half space. In this discussion, θ refers to the angle measured from the target surface ($\theta = -90^\circ$ corresponds to the direction straight downward, and $\theta = +90^\circ$ to the direction straight upward), and φ is the azimuth, measured away from the downrange direction ($\varphi = 0^\circ$ is the downrange direction, and $\varphi = 180^\circ$ is the uprange direction).

In the simulations, the projectile impacts the target at 15, 30, 45, 60, and 90° (vertical) from the surface. Each simulation starts with the projectile already tangent to the target surface. As a result, the details of atmospheric entry and interaction before the impact cannot be studied with these simulations.

RESULTS AND DISCUSSION

The thermodynamic history of the projectile was recorded through the tracer particles. Figures 1 and 2 show the pressure and temperature evolution of two projectile tracers for the various three-dimensional simulations. The tracer of Fig. 1 is located in the leading half of the projectile, close to the impact point ($\theta = -90^\circ$; $\varphi = 0^\circ$). Figure 1a shows the path followed by the tracer in the various runs. In every case, except for the highly oblique 15° simulation, the tracer remains inside the opening crater during the length of the simulation. Being so close to the impact point, the shock pressure and temperature experienced by the tracer is quite high, ranging from >500 GPa and 18 000 K for the vertical impact to >100 GPa and 2500 K for the weak, 15° impact. The shock state lasts for the time it takes the shock wave to propagate through the projectile, reflect at the rear or top free surfaces, and travel back through the projectile as a rarefaction wave that releases the material from the shock state. This length of time roughly corresponds to the time required for the projectile to traverse a distance equal to its own diameter into the target; for oblique impacts, it is defined by the relation $\tau = D/(v \sin \Theta)$ (Melosh, 1989), ranging from ~0.5 to ~2 s for a projectile 10 km in diameter impacting at angles between 90° and 15° . The tracer in Fig. 2 is located in the trailing half of the projectile ($\theta = +90^\circ$; $\varphi = 0^\circ$) and has a very different temporal

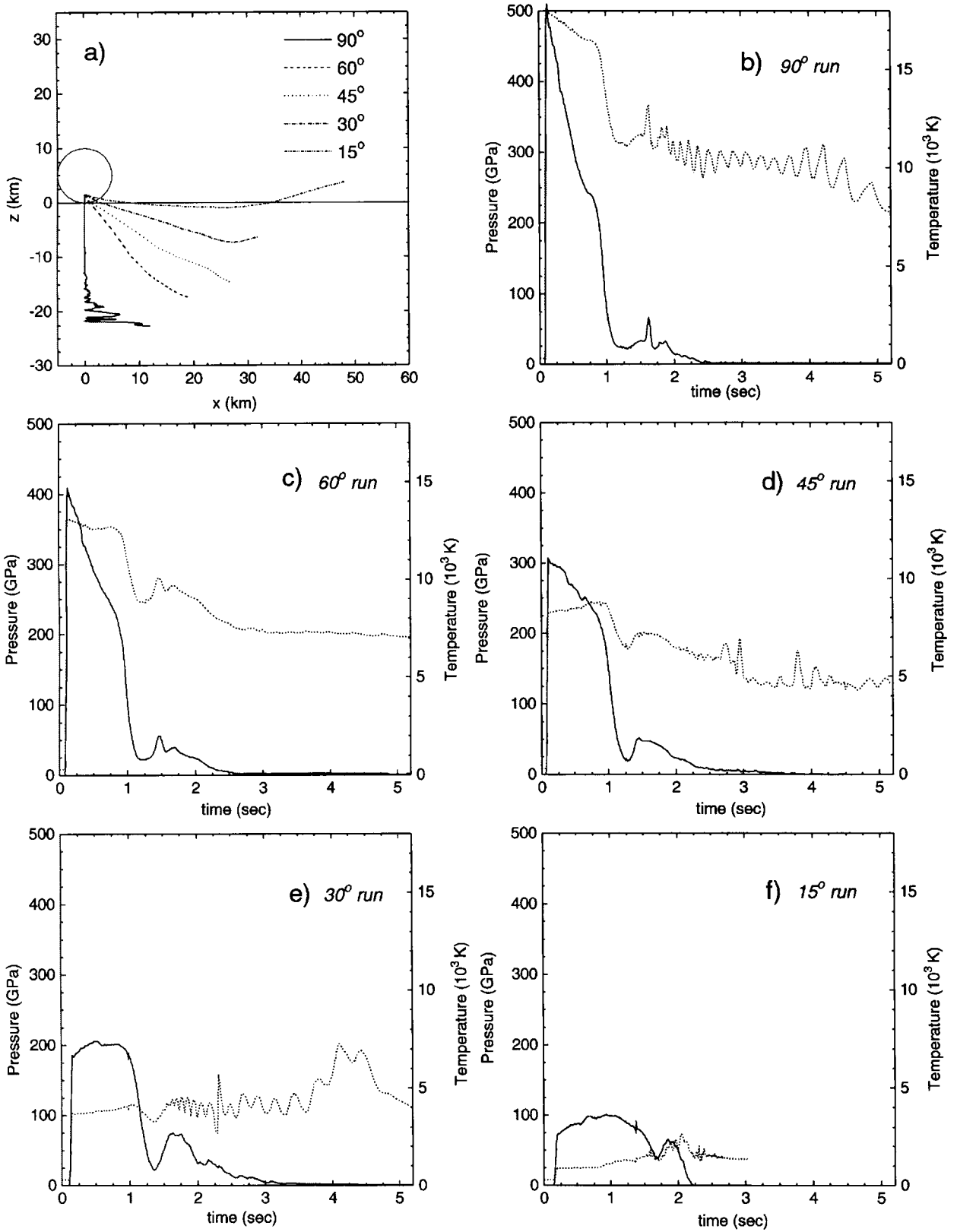


FIG. 1. Path, pressure, and temperature histories for a tracer particle located in the leading half of the projectile, close to the impact point, for the 90, 60, 45, 30, and 15° simulations. In the pressure-temperature vs. time plots, a solid line represents pressure and a dotted line represents temperature.

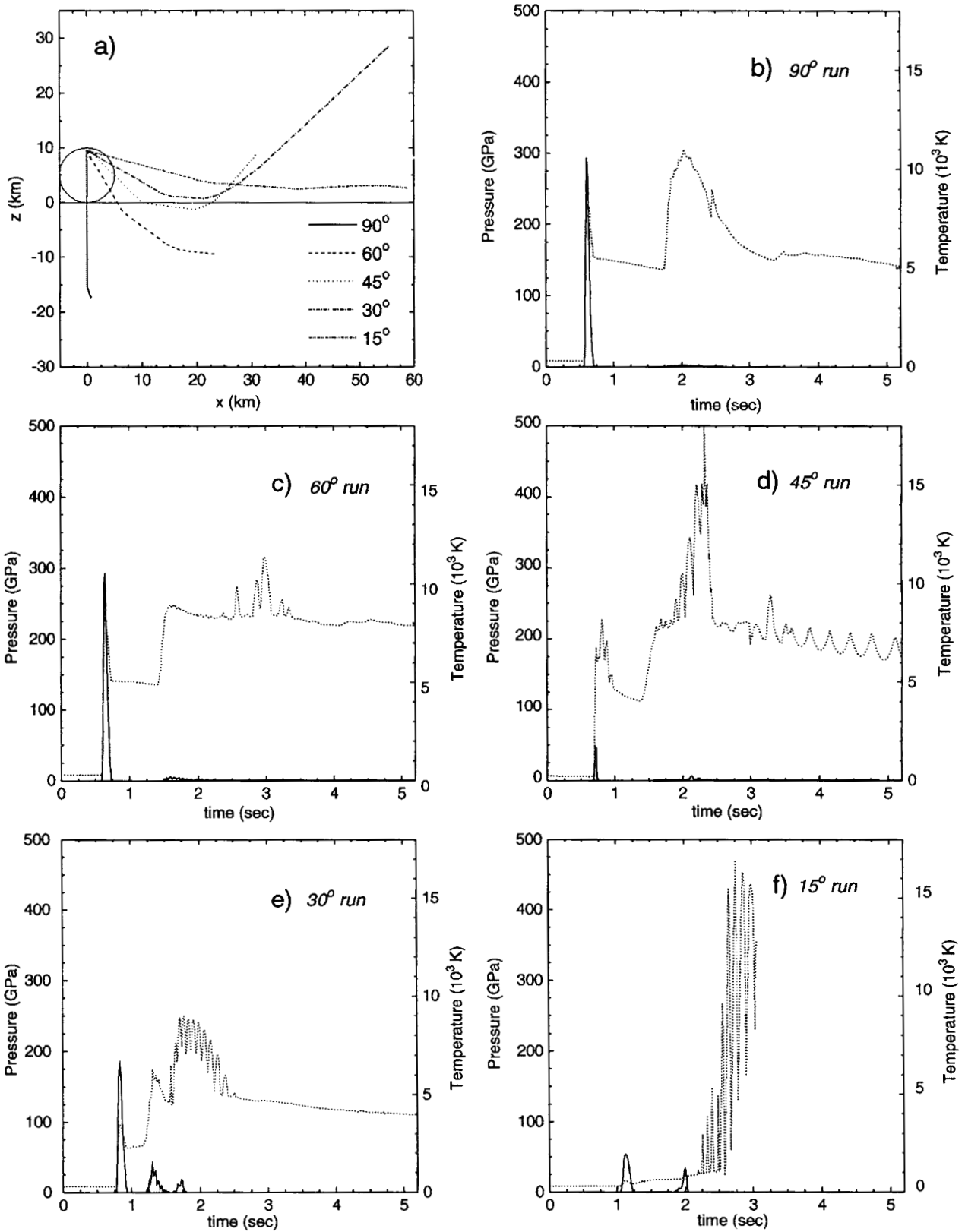


FIG. 2. Path, pressure, and temperature histories for a tracer particle located in the trailing half of the projectile, far from the impact point, for the 90, 60, 45, 30, and 15° simulations. In the pressure-temperature vs. time plots, a solid line represents pressure and a dotted line represents temperature.

evolution. Except for the low obliquity cases (vertical and 60° impacts), the tracer near the trailing edge of the impactor is ejected from the crater earlier and experiences lower shock pressures and temperatures than the tracer near the leading edge. Because it is close to the rear free surface of the projectile (where the rarefaction wave originates), the shock state for the tracer of Fig. 2 is of shorter duration than for the tracer in Fig. 1.

The pressure plots for the various impacts exhibit secondary peaks, which indicate that the tracers experience secondary shocks as they move through target material during the ejection process. The first shock occurs when the projectile first impacts the target. After the initial impact, the projectile penetrates into the target; the projectile tracers appear to coast at almost constant velocity until they encounter target material moving at substantially different velocity. This target material then creates an obstacle to the tracers' motion, altering their trajectories, and producing weak secondary shocks. Indeed, the secondary shocks for the tracers of Fig. 1 and 2 are also associated with changes in their trajectories. Besides the secondary shocks, very high temperatures are recorded by the tracers even after being ejected from the crater. In particular, large temperature fluctuations are recorded by the tracer of Fig. 2. These oscillations are due to the tracer moving through a sequence of cells in which the temperature changes wildly and therefore appear regular in frequency. We believe that these temperature oscillations reflect the presence of physical turbulence, in which material with very different thermodynamic histories are mixed in one cell, as a result of both Kelvin–Helmholtz and Rayleigh–Taylor instabilities (e.g., see O'Keefe *et al.*, 1994; Svetsov *et al.*, 1995; Crawford, 1996). The actual turbulent structure is probably not resolved by the code (the mesh setup is such that in the region where the temperature fluctuations occur, the cell size is ~ 1 km; a higher resolution in that region would probably result in a higher frequency in the temperature oscillations). Turbulence in the expansion plume also explains the higher postshock temperatures experienced by the tracer from the trailing half of the projectile as compared to the tracer from the leading half (which is still inside the opening cavity; Fig. 1) in the 45° impact. In the 30° run, the temperature fluctuations for the tracer of Fig. 2 are of short duration, probably because the tracer enters the expansion plume and is then transported into the upper atmosphere in a thermodynamically more stable region. On the other hand, in the 15° run, during its motion downrange of the impact the tracer remains close to the surface where turbulence is high and therefore it records the largest temperature fluctuations. The high temperatures through which the tracer passes correspond to material from either the other portion of the projectile, target, or the atmosphere, which were heated in the shock. The tracer in the 15° case did not itself experience a high degree of shock heating but later entered cells with strongly heated vapor. Whether and how much of the projectile would eventually melt or vaporize due to exposure to these high temperatures cannot be determined from the existing computer code.

In laboratory experiments the distribution, size, and velocity of ricocheting materials are recorded by "witness plates," which usually consist of plates or foils of Al positioned downrange of the impact point and perpendicular to the impact plane (e.g., Gault and Wedekind, 1978; Schultz and Gault, 1990a). Material that ricochets from the projectile hits the foil and leaves an imprint on it. The analysis of witness plates has provided information important to the understanding of oblique impacts. After analyzing witness plates from highly oblique impacts ($\Theta < 10^\circ$), Gault and Wedekind (1978) reached the conclusion that even for small impact velocities ricochet

material can have velocities high enough to escape the gravitational fields of planetary objects like the Moon or Mercury. In particular, Schultz and Gault (1990b) found that for impact angles $\sim 15^\circ$ or lower, the effective ricochet velocity is $>50\%$ of the impact velocity. Furthermore, the amount of projectile ricocheted increases with decreasing impact angle. Witness plates are a valuable diagnostic tool; so to compare theory and experiments, we introduced "virtual" witness plates on which we display the results of our numerical computations. The virtual witness plate was located 50 km downrange of the impact point. The trajectories of tracers that had not reached that distance by the end of the simulations were extrapolated assuming they followed straight lines at constant velocity, until they reach the witness plate. Note that, in actuality, by the end of the simulations many tracers are still moving downward inside the crater. For those tracers, the positions recorded on the virtual witness plates are not realistic, projecting well below the surface ($z < 0$). This is the case for most of the tracers of the vertical and 60° simulations, Fig. 3a and 3b, respectively. Obviously, such projectile fragments would not appear in a real witness plate. The virtual witness plates for the various simulations, Fig. 3a–e, show how projectile material is distributed downrange of the impact as function of impact angle. As shown experimentally, it is evident that as the impact angle decreases, a progressively larger amount of the projectile is ejected from the crater early in the impact event and focuses in the downrange direction. The spreading of projectile material in the y -direction seems to be independent of impact angle, whereas the spreading in the z -direction decreases with impact angle.

Velocity Distribution

The decreasing impact angle also affects the overall momentum of the projectile. The distribution of velocity is shown in Fig. 4 for the various simulations. Because of bilateral symmetry, the average velocity component in the y -direction is zero, and Fig. 4 shows the x - and z -components of the velocity vector for the projectile tracers (crosses). The average velocity vector, $\langle V \rangle = (V_x, V_z)$, at the end of the simulations, ~ 5.2 s after the impact (~ 3.2 s for the 15° case), is shown as a thick solid line. The components V_x and V_z are obtained by averaging the velocity of the projectile material: $V_{x,z} = \sum v_m^{x,z} dm$, where dm is the fraction of projectile mass with velocity $v_m^{x,z}$. The angle between the mean velocity and the velocity of the portion of the projectile dm moving with velocity v_m , is defined as $\Omega_m = (\langle V \rangle \times v_m) / (|\langle V \rangle| |v_m|)$, and it gives a measure of the scatter of the material's velocity around the mean. The mean projectile velocity and angular dispersion for the various simulations are reported in Table 1. In Fig. 4 the angular dispersion of velocity for the projectile, $\langle \Omega \rangle$, averaged over all dm , is represented by dotted lines. In the simulations, the mean angular dispersion is always $< 30^\circ$, being largest in the vertical and 60° simulations. As expected, the vertical impact simulation shows a velocity distribution with a net downward direction and no detectable horizontal momentum (Fig. 4a). As the angle of impact decreases, however, the velocity distribution shows an increasing downrange and upward component, the downrange component becoming dominant in the 15° simulation (Fig. 4e). The overall downrange momentum of the projectile in oblique impacts is also responsible for the opening of the crater downrange of the impact point (in the vertical impact the crater is symmetric with respect to the impact point).

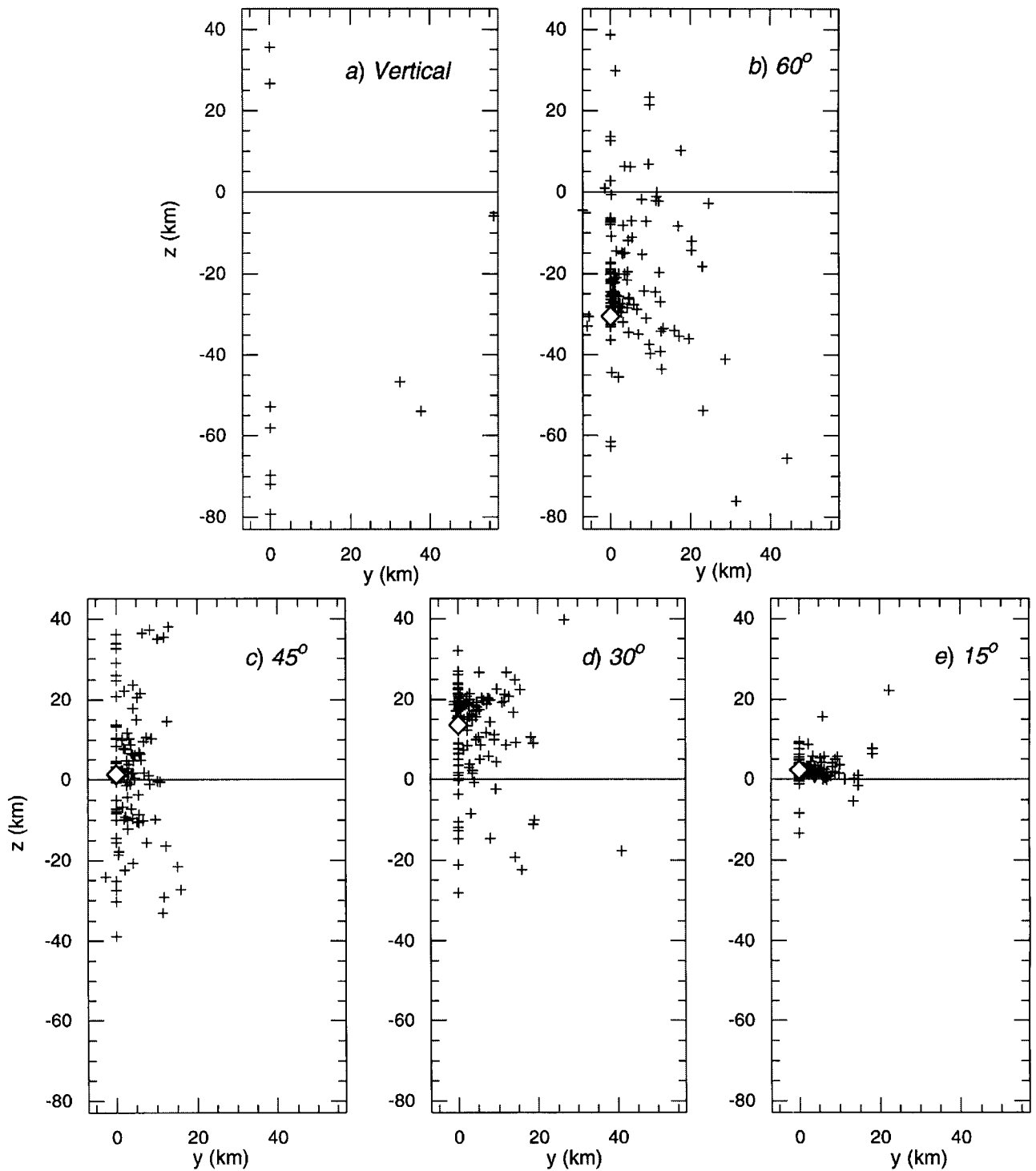


FIG. 3. Appearance of "virtual" witness plates perpendicular to the impact plane, located 50 km downrange from the impact point, for the (a) vertical, (b) 60° , (c) 45° , (d) 30° , and (e) 15° simulations. Only projectile tracers are shown (crosses). A diamond represents the mean position for all the projectile tracers; such position is well outside the view in the vertical case (a).

Finally, as observed experimentally (*e.g.*, Gault and Wedekind, 1978; Schultz and Sugita, 1996), for very oblique impacts downrange velocities can exceed the initial impact velocity; in the 30° and 15° simulations, a significant amount of projectile carries velocities larger than the escape velocity for the Earth. Even in the

45° and 60° simulations, the downrange velocity, although well below the escape velocity, is still significant, which suggests that except maybe for the vertical case it is improbable that any significant amount of projectile will remain inside the crater in large impact events.

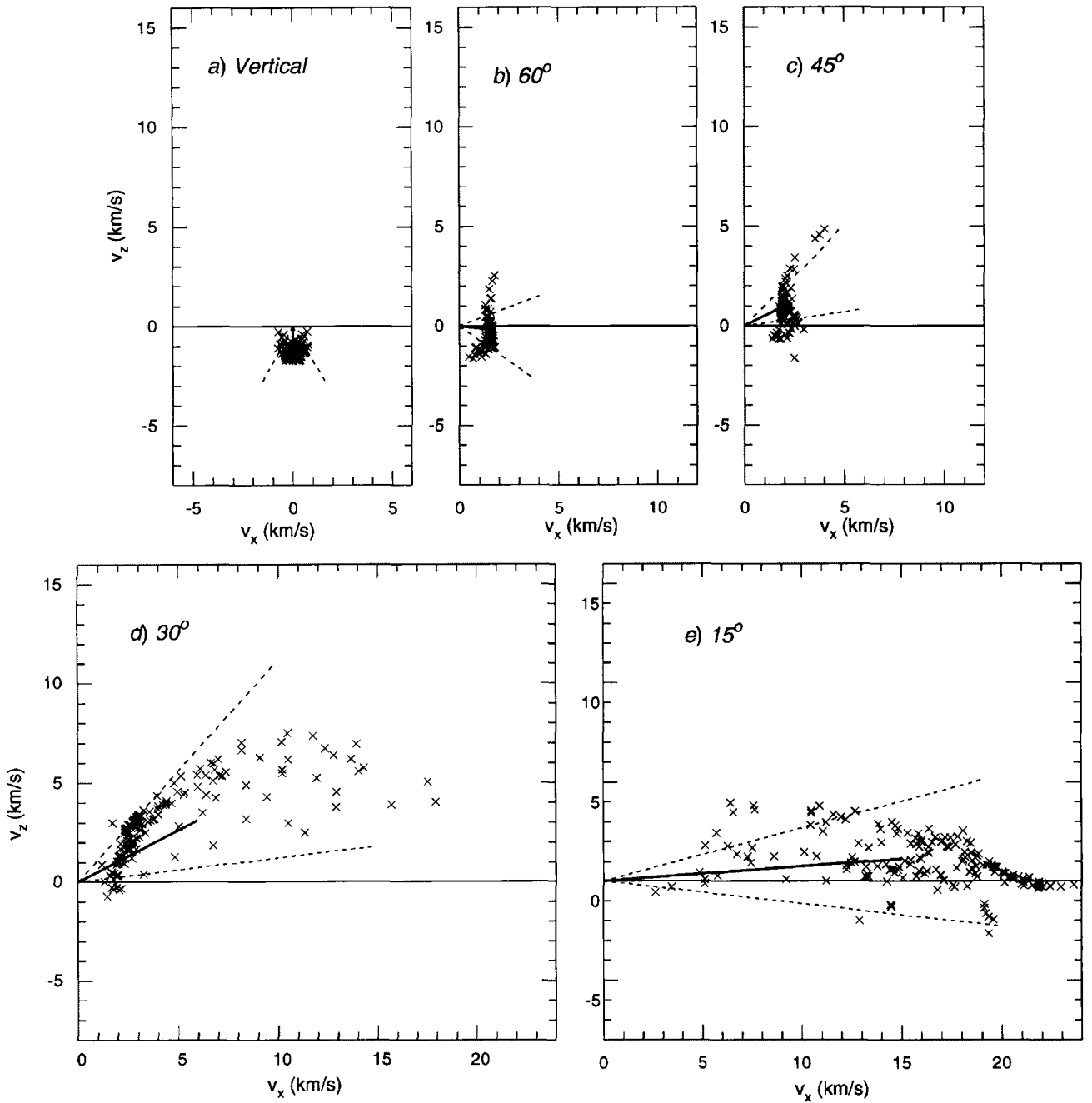


FIG. 4. Projectile postimpact velocity (crosses) in the plane of impact for the (a) vertical, (b) 60°, (c) 45°, (d) 30°, and (e) 15° simulations. Thick solid lines represent the mean velocity vector $\langle V \rangle$. Due to bilateral symmetry, the y -component of the mean velocity is zero. Dotted lines represent the mean angular dispersion $\langle \Omega \rangle$ of the projectile velocity. The projectile downrange focusing as the impact angle decreases is clear.

TABLE 1. Mean projectile velocity and relative angular dispersion for the various simulations ($\pm 1\sigma$).

Impact angle	$\langle V_x \rangle$ (km/s)	$\langle V_z \rangle$ (km/s)	$\langle \Omega \rangle$ (degrees)
90°	0.0 ± 0.8	-1.1 ± 1.2	29.7
60°	1.5 ± 2.0	-0.2 ± 1.9	28.0
45°	2.3 ± 3.4	1.1 ± 2.9	18.3
30°	5.9 ± 12.6	3.1 ± 5.2	20.6
15°	15.0 ± 21.0	1.1 ± 2.9	10.8

Strength of the Shock *versus* Impact Angle

The distribution of peak shock pressure, temperature, and energy inside the projectile are summarized in Figs. 5, 6, and 7, respectively, for the various simulations. The distributions relative to an equivalent two-dimensional hydrocode simulation (using CSQ; Pierazzo *et al.*, 1998) are also shown (Figs. 5a, 6a, and 7a) to compare the outcome of two-dimensional (dot-dashed line) and vertical three-dimensional (solid line) simulations. The two-dimensional simulation is only capable of modeling a vertical impact, which we compare to the three-dimensional vertical impact as a test of the validity of the two

hydrocodes. However, it must be pointed out that although the input layout and resolution used are the same, the two-dimensional simulations use better equations of state (determined using ANEOS) than the three-dimensional simulations (that use available SESAME equations of state). Figures 5a, 6a, and 7a show that the two-dimensional simulations tend to underestimate the peak shock pressure and energy and to overestimate the peak shock temperature. However, it is not clear if this difference is intrinsic to the code (two-dimensional vs. three-dimensional) or if it is merely due to the differences in equations of state. Recently, a similar two-dimensional vs. three-dimensional effect in hydrocodes was pointed out by Thomas and Brookshaw (1997). They run two- and three-dimensional simulations using their smoothed particle hydrodynamic (SPH) code and, similar to this work, found that the two-dimensional simulation overestimated the peak shock temperature. Their study suggested a temperature difference of as much as an order of magnitude between the two- and three-dimensional simulations. However, because of the lower resolution used in their three-dimensional simulations, the two simulations cannot be considered equivalent (the importance of the resolution in hydrocode simulations is addressed in Pierazzo *et al.*, 1997). On the other hand, this work indicates that the temperature difference is less than a factor of 2 between our equivalent two- and three-dimensional simulations, which are characterized by similar resolution. As a result, although the evidence seems to suggest that a resolution effect might be the main factor at play in Thomas and Brookshaw (1997) study, a dimensional effect in the hydrocodes (*i.e.*, the addition of a third dimension) cannot be rigorously ruled out yet.

Experimental work (Gault and Wedekind, 1978) suggests that cratering efficiency is directly proportional to $\sin \Theta$, as if only the vertical component of the impact velocity were effective in cratering. This result led Schultz and Gault (1990b) to suggest that the peak shock pressure also depends on this component alone. A simple look at the Hugoniot equations, which describe the shock, shows that both shock pressure and shock energy are proportional to particle velocity squared. Temperature is directly proportional to energy; therefore, it is proportional to particle velocity squared as well. If we assume that only the vertical component of the impact velocity contributes to the impact event, shock pressure and temperature should depend on $\sin^2 \Theta$. Figure 5b–e shows the distribution of the peak shock pressure for the various oblique runs inside the projectile (solid line). When compared to the distribution for the three-dimensional vertical impact, a dependence on $\sin \Theta$ emerges. The dashed lines in Fig. 5b–e are obtained by multiplying the peak shock pressure in the projectile for the three-dimensional vertical run by $\sin \Theta$. The agreement of the scaled distribution with the distributions from the oblique runs is good overall, with the exception of the 15° run, for which the scaled distribution overestimates that from the oblique simulation. This agreement is summarized in Fig. 8a, which shows the mean peak shock pressure inside the projectile vs. impact angle. We determined the peak shock temperature and internal energy at the time of the maximum shock pressure. The peak shock temperature (Fig. 6) and energy (Fig. 7) distributions in the projectile for the various oblique simulations show a dependence on $\sin^{3/2} \Theta$. The dashed lines in Fig. 6b–e are obtained by multiplying the temperature in the three-dimensional vertical impact by $\sin^{3/2} \Theta$. This scaled distribution is in good agreement with the oblique impact distributions for angles down to 45° (Fig. 6b–c), although it slightly overestimates the peak

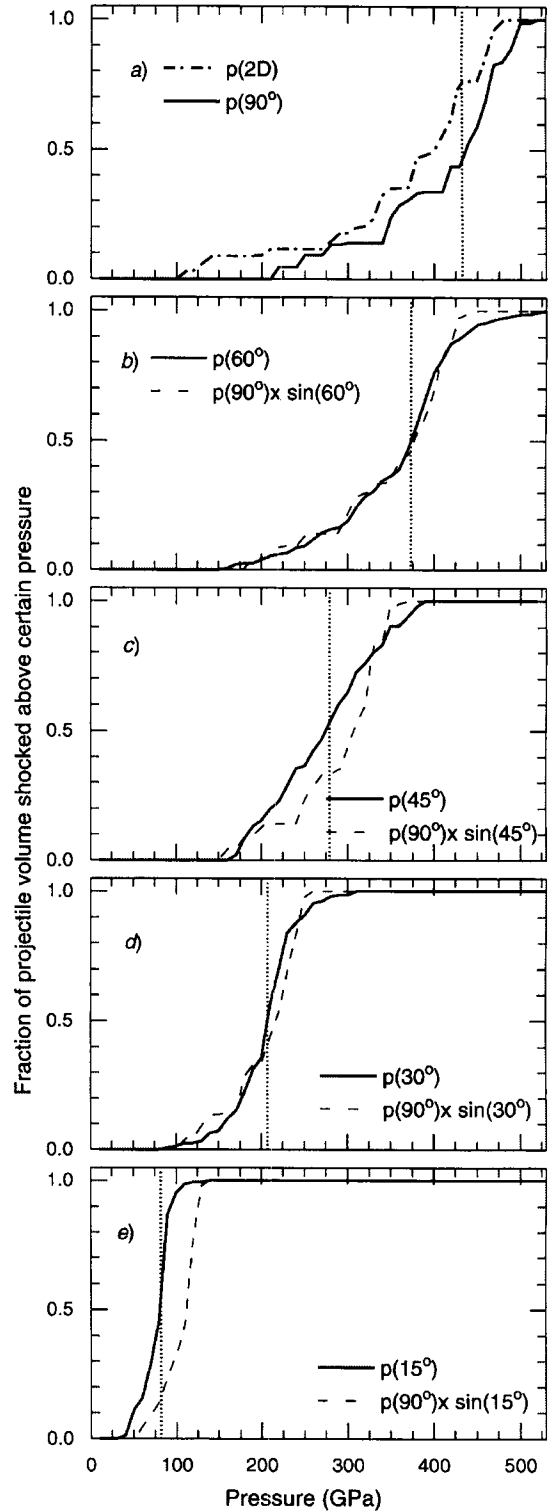


FIG. 5. Maximum shock pressure distribution in the projectile for the various simulations. (a) Comparison between the three-dimensional vertical (solid line) and an equivalent two-dimensional simulation (dot-dashed line) (Pierazzo *et al.*, 1998); (b), (c), (d), and (e) are comparisons between the 60, 45, 30, and 15° simulations (solid lines), respectively, and the vertical simulation scaled by $\sin \Theta$ (dashed line), where Θ is the impact angle. The vertical dotted line indicates the median of the (solid line) distribution. Note that as the impact angle decreases, the average shock pressure in the projectile decreases as well.

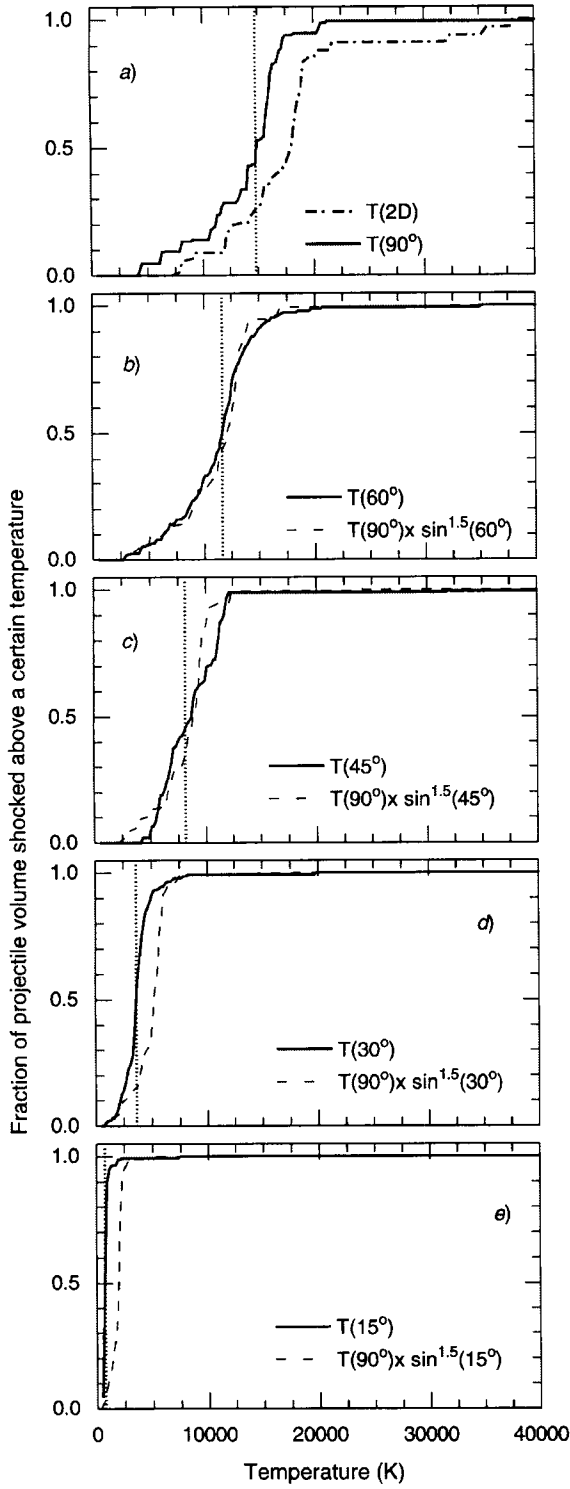


FIG. 6. Maximum shock temperature distribution in the projectile for the various simulations. (a) Comparison between the three-dimensional vertical (solid line) and an equivalent two-dimensional simulation (dot-dashed line) (Pierazzo *et al.*, 1998); (b), (c), (d), and (e) are comparisons between the 60, 45, 30, and 15° simulations (solid lines), respectively, and the vertical simulation scaled by $\sin^{3/2} \Theta$ (dashed line). The vertical dotted line indicates the median of the (solid line) distribution. Note that as the impact angle decreases, the average shock temperature in the projectile decreases as well.

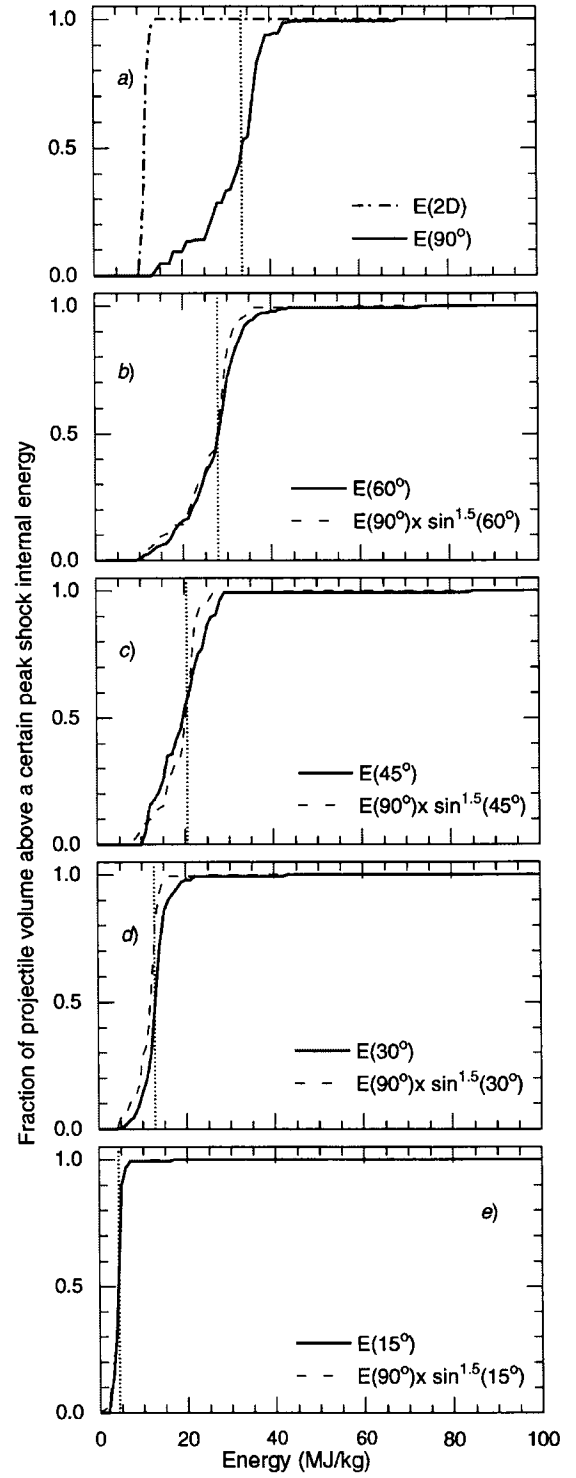


FIG. 7. Maximum shock energy distribution in the projectile for the various simulations. (a) Comparison between the three-dimensional vertical (solid line) and an equivalent two-dimensional simulation (dot-dashed line) (Pierazzo *et al.*, 1998); (b), (c), (d), and (e) are comparisons between the 60, 45, 30, and 15° simulations (solid lines), respectively, and the vertical simulation scaled by $\sin^{3/2} \Theta$ (dashed lines). The vertical dotted line indicates the median of the (solid line) distribution. Note that as the impact angle decreases, the average shock energy in the projectile decreases as well.

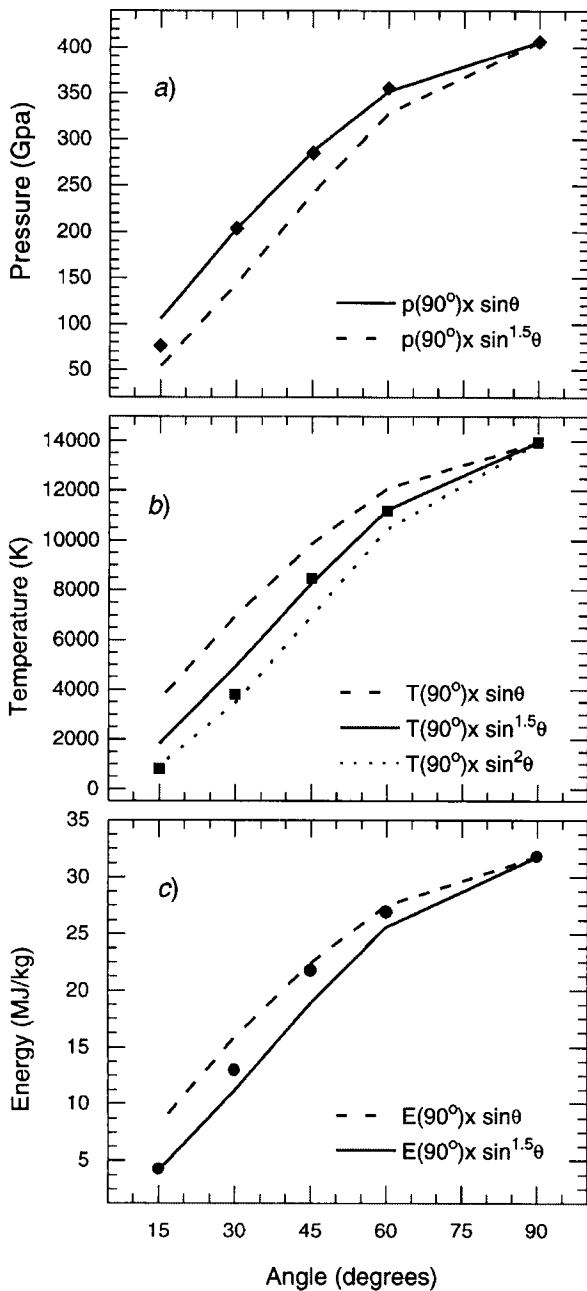


FIG. 8. Mean shock pressure (a), temperature (b), and energy (c) vs. angle of impact. Solid symbols represent the outcome of the hydrocode simulations; lines represent the scaling from the three-dimensional vertical case using $\sin^\alpha \Theta$ with $\alpha = 1$ for the shock pressure (a), and $\alpha = 3/2$ for the shock temperature (b) and energy (c).

shock temperature at lower impact angles (Fig. 6d–e). The peak shock energy distribution, however, show a generally good agreement with $\sin^{3/2} \Theta$ (Fig. 7b–e). Figure 8b–c shows the mean shock temperature and internal energy for the projectile vs. impact angle for the various oblique impacts compared to the scaled 90° .

A geologically important parameter related to impact events is the residual temperature, which is the temperature in the material after the shock has passed. As these simulations only cover the first 5 s of the impact, they cannot provide an estimate of the final residual temperature. Indeed, two-dimensional hydrocode simulations suggest

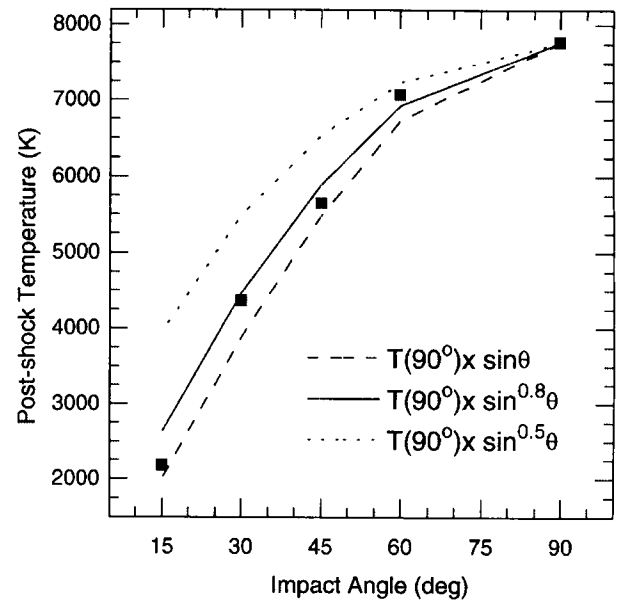


FIG. 9. Average postshock temperature vs. angle of impact. Solid symbols represent the outcome of the hydrocode simulations. Lines represent the scaling from the three-dimensional vertical case using $\sin^\alpha \Theta$: dotted line for $\alpha = 0.5$; solid line for $\alpha = 0.8$; dashed line for $\alpha = 1$.

that the temperature reaches a plateau only after ~ 10 s (Pierazzo *et al.*, 1998). It is possible, however, to estimate the postshock temperature, a value that identifies the immediate temperature drop in the material after the rarefaction wave has unloaded the material from the shock state. Even though the postshock temperature is not the same as the residual temperature, its scaling with impact angle can be used to represent the temperature scaling away from the shock state. Figure 9 shows the projectile postshock temperature (averaged over the last 2 s of the simulations, with the exception of the shorter 15° impact simulation, for which the average covers only a few tenths of a second) for the various simulations. The postshock temperature shows a less steep decrease with impact angle than the shock temperature (Fig. 8b). Indeed, scaling of the three-dimensional vertical case seems to best represent the impact angle dependence if a sine to the 0.8 power is used, instead of the $3/2$ power needed to scale the shock temperature.

These results demonstrate that in impact events the shock wave, which propagates through projectile and target material, is a function of complex processes that cannot be described by simple empirical rules. The vertical component of the impact velocity alone does not account for the strength of the shock wave generated by the impact, suggesting that more work, both experimental and theoretical, is needed to understand oblique impacts. Although this result does not affect the mechanical aspects of the impact event (*i.e.*, the opening and final size of the crater), it might have important repercussions for the thermodynamics of the impact event and influence processes like the expansion plume or melting and vaporization in both target and projectile.

Melting and Vaporization in the Projectile

The peak shock pressure experienced by each projectile tracer was used to reconstruct and evaluate the amount of projectile material that underwent melting or vaporization. The method used to determine the amount of melt and vapor produced is similar to that used for two-dimensional simulations (*e.g.*, Pierazzo *et al.*, 1998). For each row of tracers identified by a set of angles (θ , ϕ_i),

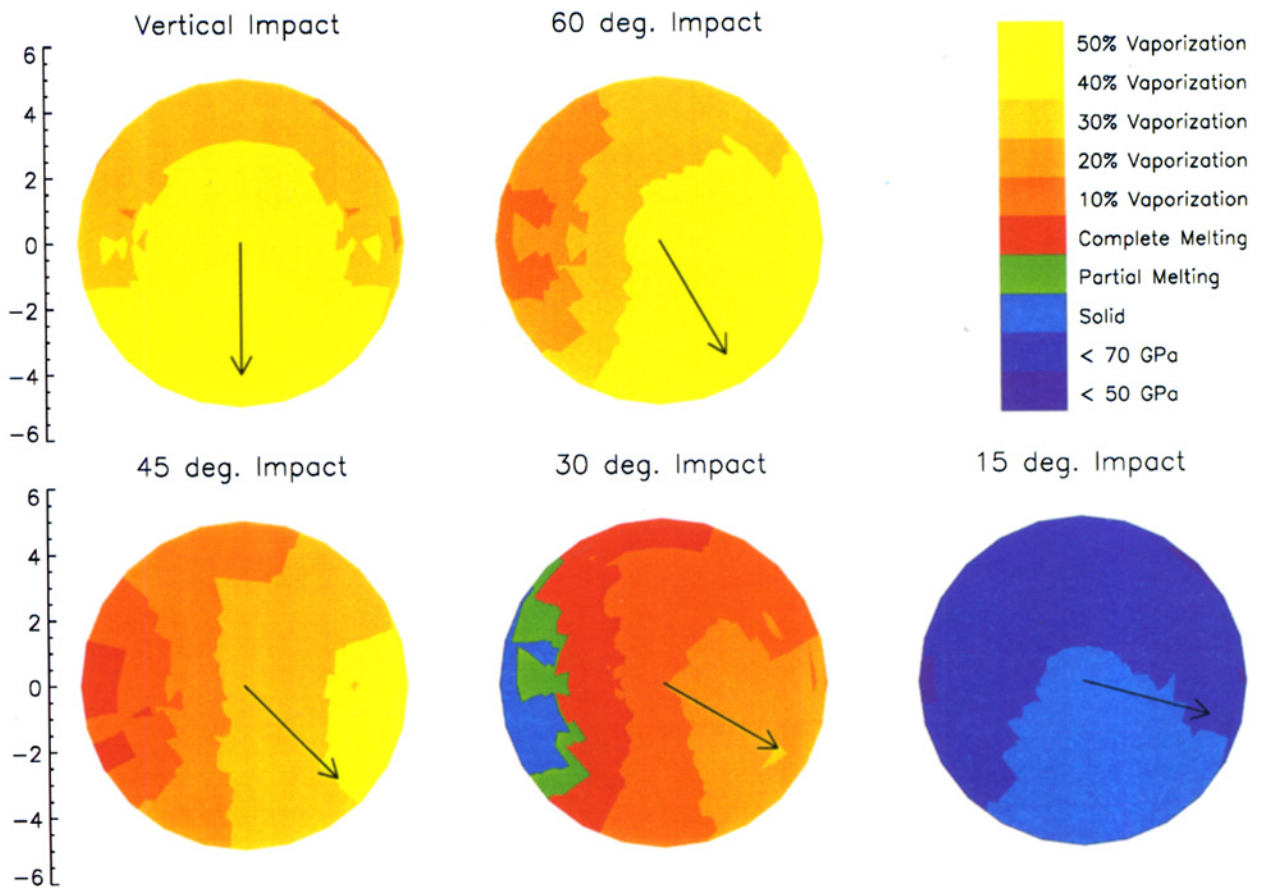


FIG. 10. Distribution of shock melting and vaporization inside the projectile for the various hydrocode simulations. To show the shock state inside the projectile for the 15° simulation, regions with shock pressures lower than 70 and 50 GPa are also shown. Vectors represent the direction of impact in the various cases.

the peak shock pressure experienced by each tracer was extracted and used to calculate the position at which the shock pressure equals the melting and vaporization pressures. The positions of these transitions along the rows of tracers were then used to construct a surface in three-dimensions bounding the volume of material melted or vaporized. We estimate that this technique introduces an uncertainty of ~10% in the final volume estimates. This uncertainty arises from representing a complex curved surface by a collection of planar triangles.

Just as we found for the target (Pierazzo and Melosh, 1998), the distribution of shock pressure inside the projectile differs between the uprange and the downrange directions. This is shown in Fig. 10, which represents the distribution of melting and vaporization in the plane of the impact (plane perpendicular to the target surface that includes the projectile's line of flight) for the various simulations (vectors indicate the impact direction). The shock pressure is highest in the leading half of the projectile, where most of the vaporization occurs (especially for the more oblique impacts). Because the shock weakens with distance from the impact point, the trailing half of the projectile is subjected to a weaker shock. As a result, any component of the projectile surviving in the solid state is bound to come from the trailing half. Furthermore, the presence of free surfaces at the sides and back of the projectile permits rarefaction waves to propagate toward the impact point and thus results in a complex pattern of stresses in the projectile, which is also complicated by the impact geometry for oblique impacts. This

results in a distribution of the peak shock pressure (and therefore of the regions of melting and vaporization) that is not symmetric with respect to the direction of impact.

The amount of projectile melted, vaporized, and in solid state vs. angle of impact is shown in Fig. 11 and summarized in Table 2. Similarly to what happens in the target (Pierazzo and Melosh, 1999), the simulations indicate a drastic decrease in shock melting and vaporization of the projectile for low impact angles, resulting in no melting for the 15° case. This effect is due to the decrease of shock pressure with angle of impact (Fig. 5); indeed between the 30 and 15°, the shock pressure falls below the threshold for shock melting of the projectile material. Little projectile vaporization occurs in the 30° simulations. Although still limited to <50% of the projectile mass, vaporization increases dramatically in the vertical and 60° simulations.

These results allow us to make qualitative estimates of shock melting and vaporization for various types of projectiles in oblique impact events. The estimates of Table 2 (Fig. 11) apply to a dunite projectile at full density. Dunite is representative of mantle material, and it is a reasonable approximation for asteroidal composition, which, on average, is mafic or ultramafic. Crystalline dunite, characterized by density ~3.3 g/cm³, has shock melting pressures >100 GPa (incipient melting = 135 GPa; complete melting = 149 GPa; incipient vaporization = 186 GPa; Pierazzo *et al.*, 1997; also see Benz *et al.*, 1989, for the ANEOS equation of state of dunite). Asteroids, however, have densities estimated between 1.6 and

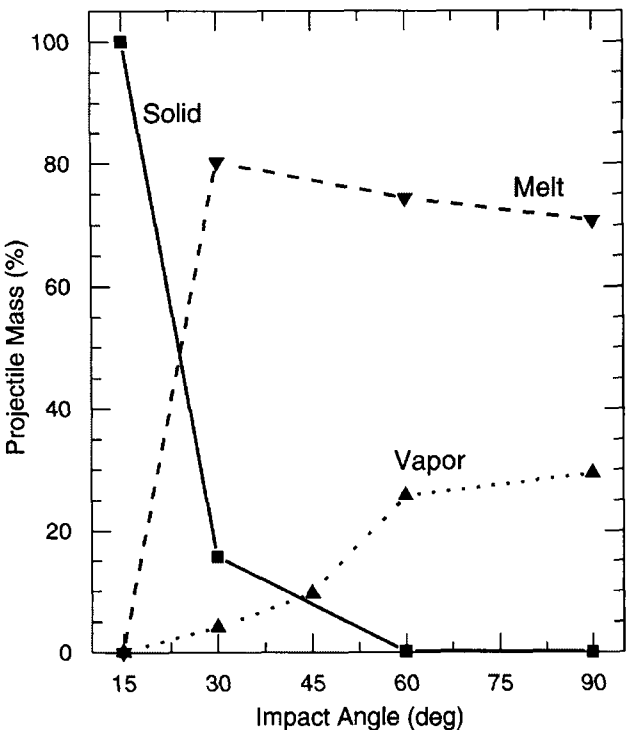


FIG. 11. Amount of projectile in solid (solid line, squares), melt (dashed line, down-triangles), and vapor (dotted line, up-triangle) state after the shock. Symbols represent the outcome of the hydrocode simulations.

2.6 g/cm³ (e.g., see Britt and Consolmagno, 1996; Corrigan *et al.*, 1996) and are characterized by a high degree of porosity. Porosity tends to lower the melting and vaporization shock pressures (Kieffer, 1971; Ahrens and O’Keefe, 1972; Kieffer *et al.*, 1976; also see the review by Grieve *et al.*, 1998); therefore, it is reasonable that a stony asteroid would partially melt down to very low impact angles. However, vapor production is still limited, perhaps becoming dominant only for vertical impacts (complete vaporization shock pressure for crystalline dunite is >2000 GPa). On the other hand, for an iron asteroid the amount of melting and vaporization is only a fraction of the values given in Table 2 (for Fe, the experimentally measured shock pressure for incipient melting is 242 GPa; Bass *et al.*, 1987; ANEOS’ estimated incipient melting for pure Fe is ~310 GPa, and incipient vaporization ~800 GPa; e.g., Pierazzo *et al.*, 1998), which suggests that little, if any, vaporization would occur even for vertical impacts. The only event in which most of the projectile could vaporize even at low impact angles is a cometary impact. Indeed, complete vaporization for ice occurs at shock pressures <100 GPa (e.g., Ahrens and O’Keefe, 1985; Blank and Miller, 1997), so that most of the cometary ice would vaporize even for very low impact angles.

The general belief that the impactor almost entirely vaporizes in impact events must then be reevaluated. Kyte (1998) concludes, on the basis of both the composition of the micrometeorite found at the K/T boundary of a DSDP core (Hole 576) and the low probability of survival of cometary material in solid state, that the K/T impactor was an asteroid. This work suggests that a large fraction of the K/T impactor, if it was an asteroid, may have melted and not vaporized if the impact was sufficiently oblique and if some portions of the projectile remained in the solid state. Even though it is not vaporized, the projectile may still have been rapidly expelled from

TABLE 2. Percentage of impactor in the solid, liquid and vapor state.

Impact Angle	Solid (%)	Melt (%)	Vapor (%)
90°	0.0	71	29
60°	0.07	74	26
45°	90*		10
30°		80	4
15°	100	0.0	0.0

*Combination of melt and solid; an unfavorable tracer distribution in this run did not allow a clear discrimination of melt regions and solid regions.

the crater by the expanding vapors from the shocked target. The existence of pieces of the asteroid that survived the impact event in solid phase is then a normal outcome for typical oblique impacts.

Shear Heating in the Projectile

The numerical computations reported here assume that neither the projectile or target material possess any intrinsic strength. This is clearly an oversimplification and could potentially lead to incorrect results, especially in view of Schultz (1996) observation that shear heating plays an important role in his laboratory-scale experiments. Although we cannot definitively evaluate the effect of strength in the projectile without new computer runs that incorporate strength, we can establish some bounds on how important the process may be in affecting the final state of the projectile.

In the worst case, shear is homogeneously distributed throughout the projectile as it impacts the target and rebounds. After the initial shock, material in the projectile gradually distorts due to slightly different final velocities at different positions in the projectile. If the projectile is strong, with strength *Y*, this distortion dissipates energy in the material at the rate $\dot{E} = Y\dot{\epsilon}$ per unit volume. This energy ultimately derives from the initial kinetic energy of the projectile, so that considerable energy is potentially available through this process.

Shear heating, however, is self-limiting in the sense that, as the temperature of the projectile rises, its strength decreases and so does the rate of shear heat deposition. When the material melts its strength decreases drastically and shear heating effectively stops. Thus, although shear may cause portions of the projectile to melt, it cannot induce vaporization.

It is easy to estimate how much distortion is necessary to cause melting. A widely used parameterization (e.g., see the review by Anderson, 1987) is to set the yield strength of the material equal to a decreasing function of the internal energy E , $Y = Y_0 (1 - E/E_m)^n$, where E_m is the internal energy at melting per unit volume and *n* is a parameter usually chosen to be either 1 or 2. Integration of the total energy dissipated indicates that complete melting occurs at a final total strain $\epsilon_{melt} = E_m/Y_0$ for *n* = 2. Using typical values for silicate bodies, $E_m \approx 9 \times 10^9$ J/m³, and $Y_0 \approx 1$ GPa, we find that melting occurs after a strain of ~10 has accumulated.

It is thus possible that melting may occur in some of the most distorted regions of the projectile (most likely to be at the projectile-target interface). In the case of very low angle impacts, such as our 15° simulation, this may lead to much more melting than our computations indicate. However, another factor may act to limit such melting. This factor is the well-known tendency for shear in rapidly deformed materials to concentrate in narrow shear bands (Grady, 1980; Gruntfest, 1963). Such localized shearing leads to

pseudotachylite formation in the basement rocks of impact craters (Reimold, 1995; Spray and Thompson, 1995) and may well occur in the (unobserved) projectile as well. In this case, however, the melt is not homogeneously distributed throughout the sheared material but is instead concentrated in narrow zones. Because the width of these zones is controlled by the rate of thermal conduction, they may be only millimeters or centimeters wide.

The effect of concentrating shear in narrow zones is to relieve differential stresses in the adjacent material and sharply reduce the apparent strength of the overall mass. In this case, the total amount of melt produced is small because it is confined to narrow regions and the effective stress is low. This case then corresponds closely to the conditions assumed in our numerical computations, where we set the bulk shear strength to zero. The formation of narrow shear zones then prevents differential stresses from rising very high and keeps bulk shear heating to a minimum. The net result of a low angle impact may then be a largely unmelted projectile in which deviatoric stresses are relieved by slip on a network of narrow melt-filled faults.

The two models of a strong, homogeneously deformed projectile in which shear heating may play an important role and that of a projectile cut by narrow shear bands form extreme limiting cases between which the truth must lie. Numerical studies of the shear band model are extremely difficult because the shear bands form at a scale much smaller than any practical mesh. We believe that the truth is closer to the second case and so are justified in neglecting material strength, but future investigations must be performed to demonstrate the truth of this proposal.

CONCLUSIONS

A series of high-resolution three-dimensional hydrocode simulations covering the first few seconds of the impact event have been carried out, and the fate of the projectile has been investigated as function of the angle of impact. Overall, the results are in agreement with results from experimental work (Gault and Wedekind, 1978; Schultz and Gault, 1990b; Schultz and Sugita, 1996).

The main results of this study are:

- (1) A downrange focusing of projectile material occurs in oblique impacts, becoming predominant for low impact angles. Although at the end of the hydrocode simulations the projectile is mostly smeared along the crater walls in vertical and slightly oblique (60°) impacts, in low impact angles ($\leq 30^\circ$) most of the projectile is ejected from the opening crater in the early stages of the impact.
- (2) In the vertical and 60° impacts, most of the projectile is still inside the crater, carrying a net downward motion at the end of the simulations. However, in very oblique impacts (30 and 15°), a significant amount of projectile material carries a downrange/upward velocity larger than the escape velocity of the Earth.
- (3) The shock inside the projectile weakens as the angle of impact decreases from the vertical. A crude linear dependence of shock pressure on the sine of the impact angle, $\sin \Theta$, is found (Figs. 5 and 8a), whereas shock temperature and energy show a dependence on $\sin^3 \Theta$ (Fig. 8b and c, respectively). This result suggests that the shock produced by impact events is the result of complex processes that cannot be described by simple (more or less empirical) rules.
- (4) Shock melting and vaporization occur inside the projectile for all impacts except for the most oblique, the 15° impact (Fig. 10

and Table 2). Vaporization inside the projectile decreases with angle of impact, and it occurs mainly in the leading half of the projectile (Fig. 10). The shock is weakest in the trailing half of the projectile, where any component of the projectile surviving the impact in the solid state originates. The angle of impact, therefore, influences the amount of projectile vaporization and melting. For the most probable angle of impact, 45°, <50% of the projectile mass is vaporized.

Although our understanding of oblique impacts is still incomplete—especially regarding the fate of the projectile—this systematic work has provided some simple rules to scale the more common vertical impact studies and take the angle of impact into account.

Acknowledgments—The research was supported by NASA grants NAGW-5159 and NAGW-428. The three-dimensional simulations using the CTH hydrocode were kindly performed by Dr. David Crawford using parallel computing resources located at Sandia National Laboratories, and following material and geometry description provided by the author. We are indebted to Dr. M. J. Cintala and Prof. P. H. Schultz for their accurate and very useful reviews.

Editorial handling: R. A. F. Grieve

REFERENCES

- AHRENS T. J. AND O'KEEFE J. D. (1972) Shock melting and vaporization of lunar rocks and minerals. *The Moon* **4**, 214–249.
- AHRENS T. J. AND O'KEEFE J. D. (1985) Shock vaporization and the accretion of the icy satellites of Jupiter and Saturn. In *Ices in the Solar System* (ed. I. Klinger, D. Benest, A. Dollfus and R. Smoluchowski), pp. 631–654. Kluwer Academic Press, Dordrecht, The Netherlands.
- ALVAREZ L. W., ALVAREZ W., ASARO F. AND MICHEL H. V. (1980) Extraterrestrial cause for the Cretaceous–Tertiary extinction. *Science* **208**, 1095–1108.
- ANDERSON C. E. (1987) An overview of the theory of hydrocodes. *Int. J. Impact Engineering* **5**, 33–59.
- BASS J. D., SVENDSEN B. AND AHRENS T. J. (1987) The temperature of shock compressed iron. In *High-Pressure Research in Mineral Physics* (eds. M. H. Manghnani and Y. Syono), 393–402. Terra Scientific Publ., Washington, D.C., USA.
- BENZ W., CAMERON A. G. W. AND MELOSH H. J. (1989) The origin of the Moon and the single-impact hypothesis III. *Icarus* **81**, 113–131.
- BLANK J. G. AND MILLER G. H. (1997) The fate of organic compounds in cometary impacts. In *International Symposium on Shock Waves 21st* (eds. A. Paul and F. Houwing). World Scientific Press, Singapore. In press.
- BRITT D. T. AND CONSOLMAGNO S. J. (1996) Estimating porosities from bulk densities (abstract). *Meteorit. Planet. Sci.* **31** (Suppl.), A22.
- CHYBA C. F., THOMAS P. J., BROOKSHAW L. AND SAGAN C. (1990) Cometary delivery of organic molecules to the early Earth. *Science* **249**, 366–373.
- CLARK B. C. (1988) Primeval procreative comet pond. *Origins Life Evol. Biosph.* **18**, 209–238.
- CORRIGAN C. M., ZOLENSKY M. E., LONG M. AND WEIR J. (1996) Comparison of porosity and permeability in chondritic materials (abstract). *Meteorit. Planet. Sci.* **31** (Suppl.), A32.
- CRAWFORD D. A. (1996) Models of fragment penetration and fireball evolution. In *The Collision of Comet Shoemaker-Levy 9 and Jupiter* (eds. K. S. Noll, H. A. Weaver and P. D. Feldman), pp. 133–156. *IAU Coll.* **156**.
- CROFT S. K. (1985) The scaling of complex craters. *Proc. Lunar Planet. Sci. Conf.* **15th**, C828–C842.
- FELDMAN W. C., MAURICE S., BINDER A. B., BARRACLOUGH B. L., ELPHIC R. C. AND LAWRENCE D. J. (1998) Fluxes of fast and epithermal neutrons from Lunar Prospector: Evidence for water ice at the lunar poles. *Science* **281**, 1496–1500.
- GAULT D. E. AND WEDEKIND J. A. (1978) Experimental studies of oblique impact. *Proc. Lunar Planet. Sci. Conf.* **9th**, 3843–3875.
- GRADY D. E. (1980) Shock deformation of brittle solids. *J. Geophys. Res.* **85**, 913–924.
- GRIEVE R. A. F., LANGENHORST F. AND STÖFFLER D. (1998) Shock metamorphism of quartz in nature and experiment: II. Significance in geoscience. *Meteorit. Planet. Sci.* **31**, 6–35.
- GRUNTFEST I. J. (1963) Thermal feedback in liquid flow: Plane shear at constant stress. *Trans. Soc. Rheology* **7**, 195–207.

- HOLSAPPLE K. A. AND SCHMIDT R. M. (1987) Point source solutions and coupling parameters in cratering mechanics. *J. Geophys. Res.* **92**, 6350–6376.
- KIEFFER S. W. (1971) Shock metamorphism of the Coconino sandstone at Meteor Crater, Arizona. *J. Geophys. Res.* **76**, 5449–5473.
- KIEFFER S. W., PHAKEY P. P. AND CHRISTIE J. M. (1976) Shock processes in porous quartzite: Transmission electron microscope observations and theory. *Contrib. Mineral. Petrol.* **59**, 41–93.
- KRING D. A., MELOSH H. J. AND HUNTEN D. M. (1996) Impact-induced perturbations of atmospheric sulfur. *Earth Planet. Sci. Lett.* **140**, 201–212.
- KYTE F. T. (1998) A Fossil Micrometeorite from the Cretaceous-Tertiary Boundary. *Nature* **396**, 237–239.
- MCGLAUN J., THOMPSON S. L. AND ELRICK M. G. (1990) CTH: A Three-Dimensional Shock Wave Physics Code. *Int. J. Impact Eng.* **10**, 351–360.
- MELOSH H. J. (1989) *Impact Cratering: A Geologic Process*. Oxford Univ. Press, New York, New York, USA. 245 pp.
- NOLL K. S., MCGRATH M. A., TRAFTON L. M., ATREYA S. K., CALDWELL J. J., WEAVER H. A., YELLE R. V., BARNET C. AND EDGINGTON S. (1995) HST spectroscopic observations of Jupiter after the collision of comet Shoemaker-Levy 9. *Science* **267**, 1307–1313.
- NOZETTE S., LICHTENBERG C. L., SPUDIS P., BONNER R., ORT W., MALARET E., ROBINSON M. AND SHOEMAKER E. M. (1996) The Clementine Bistatic Radar Experiment. *Science* **274**, 1495–1498.
- O'KEEFE J. D., TANAKA T. AND AHRENS T. J. (1994) Penetration of large bodies into dense planetary atmospheres—Role of hydrodynamic instabilities (abstract). *Lunar Planet. Sci.* **25**, 1023–1024.
- PIERAZZO E. AND MELOSH H. J. (1999) Hydrocode Modeling of Chicxulub as an Oblique Impact Event. *Earth Planet. Sci. Lett.* **165**, 163–176.
- PIERAZZO E. AND CHYBA C. F. (1999) Amino acid survival in large cometary impacts. *Meteorit. Planet. Sci.* **34**, 909–918.
- PIERAZZO E., VICKERY A. M. AND MELOSH H. J. (1997) A reevaluation of impact melt production. *Icarus* **127**, 408–423.
- PIERAZZO E., KRING D. A. AND MELOSH H. J. (1998) Hydrocode simulation of the Chicxulub impact event and the production of climatically active gases. *J. Geophys. Res.* **103**, 28 607–28 626.
- REIMOLD W. U. (1995) Pseudotachylite in impact structures—generation by friction melting and shock brecciation?: A review and discussion. *Earth Sci. Rev.* **39**, 247–265.
- SCHULTZ P. H. (1996) Effect of Impact Angle on vaporization. *J. Geophys. Res.* **101**, 21 117–21 136.
- SCHULTZ P. H. AND GAULT D. E. (1990a) Decapitated impactors in the laboratory and on the planets (abstract). *Lunar Planet. Sci.* **21**, 1099–1100.
- SCHULTZ P. H. AND GAULT D. E. (1990b) Prolonged Global Catastrophes from Oblique Impacts. *Geol. Soc. Am., Spec. Paper* **247**, 239–261.
- SCHULTZ P. H. AND SUGITA S. (1996) Fate of the Chicxulub impactor (abstract). *Lunar Planet. Sci.* **28**, 1261–1262.
- SCHMIDT R. M. AND HOUSEN K. R. (1987) Some recent advances in the scaling of impact and explosion cratering. *Int. J. Impact Eng.* **5**, 543–560.
- SESAME '83 (1983) Report on the Los Alamos Equation-of-State Library. *LALP-83-4*, Los Alamos National Laboratory, Los Alamos, New Mexico, USA.
- SHOEMAKER E. M. (1983) Asteroid and comet bombardment of the Earth. *Ann. Rev. Earth Planet. Sci.* **11**, 461–494.
- SPRAY J. G. AND THOMPSON L. M. (1995) Friction melt distribution in a multi-ring impact basin. *Nature* **373**, 130–132.
- SVETSOV V. V., NEMTCHINOV I. V. AND TETEREV A. V. (1995) Disintegration of large meteoroids in Earth's atmosphere: Theoretical models. *Icarus* **116**, 131–153.
- THOMAS P. J. AND BROOKSHAW L. (1997) Numerical models of comet and asteroid impacts. In *Comets and the Origin and Evolution of Life* (eds. P. J. Thomas, C. F. Chyba and C. P. McKay), pp. 131–145. Springer-Verlag Press, New York, New York, USA.
- ZAHNLE K. J. AND SLEEP N. H. (1997) Impacts and the Early Evolution of Life. In *Comets and the Origin and Evolution of Life* (eds. P. J. Thomas, C. F. Chyba and C. P. McKay), pp. 175–208. Springer-Verlag Press, New York, New York, USA.